Available online at www.sciencedirect.com
SCIENCE DIRECT®
Sensors and Actuators B 94 (2003) 103–115
SENSORS AND ACTUATORS B CHEMICAL
www.elsevier.com/locate/snb

Analysis, control and augmentation of microcantilever deflections in bio-sensing systems

A.-R.A. Khaled [a], K. Vafai [b], M. Yang [b], X. Zhang [b], C.S. Ozkan [b,*]

[a] *Department of Mechanical Engineering, The Ohio State University, Columbus, OH 43210, USA*
[b] *Department of Mechanical Engineering, University of California at Riverside, Bourns Hall A305, Riverside, CA 92521, USA*

Received 19 September 2002; received in revised form 16 January 2003; accepted 29 January 2003

Abstract

The main causes for the deflection of microcantilevers embedded in micromechanical biodetection systems are investigated. The primary deflection due to the chemical reaction between the analyte molecules and the receptor coating, which produces surface stresses on the receptor side is analyzed. Oscillating flow conditions, which are the main source of turbulence, are found to produce substantial deflections at relatively large frequency of turbulence. Bimaterial effects influencing the microcantilever deflections are established analytically, and found to be prominent at a relatively low frequency of turbulence. In the absence of bimaterial effects, turbulence increases the deflection due to chemical reactions at relatively large frequency of turbulence yet it increases the noise due to the increased dynamical effects of the flow on the microcantilever. The mechanical design and optimization of piezoresistive cantilevers for detecting changes in surface stress via finite element analysis is also discussed. The introduction of stress concentration regions (SCR) during cantilever fabrication greatly enhances the detection sensitivity. Biosensing experiments based on resonance frequency shift are presented, which show that the results strongly depend on the interaction of specific analytes with the receptor surface. Finally, novel microcantilever assemblies are presented for the first time that can increase the deflection due to chemical reaction while decreasing those due to flow dynamical effects.

Keywords: Microcantilever; Bio-sensing; Piezoelectric sensor; Resonance frequency shift

1. Introduction

The rapid growth of nanotechnology has led to new horizons for the development of biosensors that are suitable for intracellular measurements and for monitoring biomolecular processes within a living cell. These biosensors have the advantage to accurately, quickly, and economically screen patients for the presence of various diseases. The development of integrated biosensors for the detection of multiple biologically significant species has led to the concept of Biochips. Biochips are defined as substrates having microarrays of bioreceptors. These biochips are known under different names in the literature as DNA biochip, DNA chip, genome chip or DNA microarray. An example of these biochips is the biological IC chip which is described in the work of [1].

Recent advances in biochips have shown that sensors based on the bending of microfabricated cantilevers have potential advantages over previously used detection methods. Biochips with mechanical detection systems use microcantilever bi-material (e.g. Au–Si) beams as sensing elements. The Au side is usually coated with a certain receptor. Upon the binding of the analyte (e.g. biological molecules, such as proteins or biological agents) with the receptor (each individual protein interacts with a unique receptor), the receptor surface is either tensioned or relieved. This causes the microcantilever to deflect and the deflection was found to be proportional to the analyte concentration. Examples of bindings in biomolecular (receptor/analyte) applications are: antibody–antigen (receptor/analyte) bindings or DNA hybridization of a pair of DNA strands (receptor/analyte) having complementary sequences [2]. The deflection is usually in nanometers and can be measured using optical techniques. Biochips having microcantilevers as sensing elements do not require external power, labeling, external electronics or fluorescent molecules or signal transduction for their operation. These types of biochips can be used in screening certain diseases such as cancer and detecting specific chemical and biological warfare agents such as botulinum toxin, anthrax, and aflatoxin.

In spite of the distinct superiority of the biochips with mechanical detection systems, they possess few disadvantages,

* Corresponding author. Tel.: +1-909-787-5016; fax: +1-909-787-2899.
E-mail address: cozkan@engr.ucr.edu (C.S. Ozkan).

0925-4005/03/$ – see front matter © 2003 Elsevier Science B.V. All rights reserved.
doi:10.1016/S0925-4005(03)00231-4

Nomenclature

List of symbols

A_e	effective area of the microcantilever subject to drag
A_m	area of receptor coating
B	length of the fluidic cell
c_m	thermal capacitance of the microcantilever
C_D	flow drag coefficient
C_∞	free stream concentration
D_e	diffusivity of analyte
E	Young's modulus
F_v	velocity correction factor
G	Gibbs free energy
h	fluidic cell thickness
h_s/h_f	height of substrate/height of self assembled monolayer
h_c	convective heat transfer coefficient
I	moment of inertia
I_s/I_f	moment of inertia of substrate/self assembled monolayer
k_{ad}	adhesion rate
k_f	effective reaction rate
k_e	Effective stiffness of the microcantilever
K_a/K_d	Association/dissociation rate
ℓ	length of the microcantilever
m_m	mass of microcantilever
m_e	effective mass of microcantilever
M	molar mass
N	number of cells
R	resistance of the peizoresistive cantilever
S	squeezing number
t	Time
t_m	microcantilever thickness
U, u	dimensionless and dimensional translational velocity
V, v	dimensionless and dimensional normal velocity
V_0	reference inlet velocity for the fluidic cell
w	width of the microcantilever
X, x	dimensionless and dimensional axial coordinate
Y, y	dimensionless and dimensional normal coordinate
z	microcantilever deflection
z_s, z_t, z_d	deflection due to surface stress, biomaterial and dynamical effects

Greek letters

β_c/β_T	amplitude of concentration/thermal expansion coefficient
Γ	mass of bound analyte per unit area
δ	upper plate motion amplitude for the fluidic cell
κ	dimensionless slope for the fluidic cell
λ	The linear density of the beam

List of symbols

π_L	piezoresistive coefficient along <110> axis
ρ_l	density of the fluid
ρ_s/ρ_f	density of substrate/self assembled monolayer
σ	surface stress
υ	Poission's ratio
ω/ω_n	turbulence frequency/natural frequency of the microcantilever

such as turbulence in the liquid flow which affects the accuracy of the measurements as shown in [2,3]. Also, the primary type of microcantilevers used in these detection systems have low sensitivity especially for low analyte concentration and variations in liquid temperature can produce unwanted deflections due to bimaterial effects as discussed by [3].

Conventional (non-piezoresistive) cantilevers are used along with an optical detection system in many conventional scanning probe systems, which require rigorous alignment of the detecting laser beam with respect to the cantilever beam. In some cases, the laser beam is aligned to hit a shiny silicon surface or a metal coated sensing area on the back of the cantilever. In a liquid cell environment, turbulence effects could result in additional three dimensional deflections of the cantilever beam which could render any detection measurements useless. In addition, the presence of focused laser beam in a liquid cell environment can result in additional thermal management issues giving rise to extraneous readings. Piezoresistive cantilevers can be utilized to avoid these problems. Alcohol detection in gases has been performed on a polymer coated cantilever by [4]. The detection of alkanethiol monolayer formation on gold coated cantilevers in gases by [5,6]. Boisen et al. (2000) have indicated the change in the surface stress as a function of ethanol concentration in water by using commercially available piezoresistive cantilevers.

The resonance frequency of microcantilevers is very sensitive to the properties of the microcantilever surface. Changes in the surface properties of the microcantilever through binding or hybridization of analytes to receptor molecules will directly influence its resonance frequency by changing the overall cantilever mass and the thickness of the binding layer [7].

In this work, microcantilever deflections are analyzed in the presence of chemical reaction at the receptor surface as well as bimaterial effects and the dynamical effect of an oscillating flow representing flow turbulence, on the micocantilever. This analysis will help in establishing the parameters that can be used in reducing the associated noise due to microcantilever deflections. Further, the effects of certain design features for piezoresistive cantilevers that can cause enhancements of the surface stress are also discussed. Finally, experiments based on measuring the resonance frequency shifts as a result of the interaction of analytes with the receptor substrate will be performed and the results will be discussed.

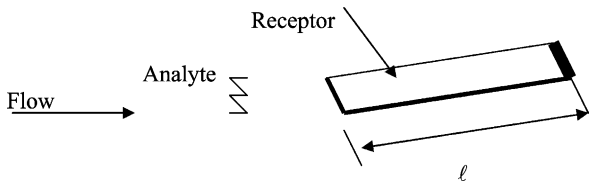

Fig. 1. Schematic illustration of an ordinary microcantilever.

2. Analysis

2.1. Deflection due to surface stresses

The deflection (z) of the tip of an ordinary microcantilever as seen in Fig. 1 can be calculated from using Stoney's equation [8]

$$z = \frac{3\ell^2(1-\upsilon)}{Et_m^2}\Delta\sigma \tag{1}$$

where ℓ, υ, E, $\Delta\sigma$, and t_m are the microcantilever's effective length, Poisson's ratio, Young's modulus, differential surface stress and its thickness.

The differential stress ΔS is proportional to the number of analytes molecules attached to the receptor surface. This relation has the following form according to [9]

$$\Delta\sigma = \Delta G \Gamma M^{-1} \tag{2}$$

where ΔG is the change in the Gibbs free energy caused by the adsorption process, Γ the mass of the bound analyte molecules per unit area and M the molar mass of the analyte. This equation is based on the Dupre equation that relates the surface free energy of the substrate and the adsorbate and the work of adhesion.

2.1.1. Rate of reaction

The first order chemical reaction equation is

$$\frac{dN_b}{dt} = k_{ad}(N_0 - N_b) \tag{3}$$

where k_{ad}, N_b and N_0 are the adhesion rate, cumulative number of bound cells and the total number of cells bound on the substrate after the experiment, respectively. The adhesion rate according to [10] is

$$k_{ad} = k_f C_\infty N_r \tag{4}$$

where k_f, C_∞ and N_r are the effective reaction rate, surface analyte concentration and the number of available receptors, respectively. The results of [11] agrees with the previous equation. Thus, Eq. (3) reduces to following

$$\frac{dN_b}{N_0 - N_b} = k_f C_\infty N_r\, dt \tag{5}$$

The analytes concentration due to turbulence can be written according to

$$C_\infty = (C_\infty)_0 - \beta_c \sin(\omega t) \tag{6}$$

where $(C_\infty)_0$ and β_c are the mean free stream analyte concentration and the amplitude of concentration. k_f increases with the vibrational frequency of the molecules [10]. Also, Ramakrishnan and Sadana show that the turbulence at the receptor surface which is produced by varying the surface roughness of the receptor results in an increase in the effective reaction rate at the surface [12]. They ascribed it to the mixing effect that the turbulence produces which results in increasing the vibrational frequency of the molecules. Turbulence at the receptor surface can also be produced by disturbances in the flow. In this work, the relation between the effective reaction rate and the turbulence frequency is taken to be linear for simplicity.

$$k_f = \bar{k}_f(1 + a\omega) \tag{7}$$

where $\bar{k}_f$ and a are the effective reaction rate in the absence of the turbulence and a constant, respectively. Thus Eq. (5) reduces to

$$\frac{dN_b}{(N_0 - N_b)} = \bar{k}_f(1 + a\omega)[(C_\infty)_0 - \beta_c \sin(\omega t)]N_r\, dt \tag{8}$$

This is a first-order differential equation and has the following solution given that $N_b(t = 0) = 0$

$$N_b = N_0[1 - e^{-\bar{k}_f N_r(1+a\omega)((C_\infty)_0 t + (\beta_c/\omega)(\cos(\omega t)-1))}] \tag{9}$$

The parameter N_b can be related to Γ by the following relation:

$$\frac{N_b}{A_m} = \Gamma M^{-1} A \tag{10}$$

where Γ, M, A and A_m are the mass of the adsorbate per unit area, molar mass, number of analyte molecules per mole and the area of the receptor coating, respectively. Therefore, the time history for the surface stress can be related to Eq. (9) by applying Eqs. (2) and (10) and the result is

$$\Delta\sigma = (\Delta\sigma)_0[1 - e^{-\bar{k}_f N_r(1+a\omega)((C_\infty)_0 t + (\beta_c/\omega)(\cos(\omega t)-1))}] \tag{11}$$

where $(\Delta\sigma)_0 = \Delta G\, N_0 A_m^{-1} A^{-1}$. Thus

$$z_s = z_0[1 - e^{-\bar{k}_f N_r(1+a\omega)((C_\infty)_0 t + (\beta_c/\omega)(\cos(\omega t)-1))}] \tag{12}$$

where $z_0 = (3\ell^2(1-\nu)/Et_m^2)(\Delta\sigma)_0$. It was found that the adhesion rate is inversely proportional to the translational velocity, u, of the analyte molecules for wide range of translational velocities. According to the data present in the work of [13], the effective binding rate can be linearly correlated to the analyte rolling velocity and the translational velocity, such that

$$\bar{k}_f = \bar{k}_{fo} - b|u| \tag{13}$$

where $\bar{k}_{fo}$ and b are constants greater than zero. Therefore, Eq. (12) is further reduced to

$$z_s = z_0[1 - e^{-(\bar{k}_{fo} - b|u|)N_r(1+a\omega)((C_\infty)_0 t + (\beta_c/\omega)(\cos(\omega t)-1))}] \tag{14}$$

when u is greatly dependent on the time, the solution to Eq. (5) is

$$z_s = z_0[1 - e^{-\int_0^1 (\bar{k}_{fo} - b|u|)N_r(1+a\omega)((C_\infty)_0 - \beta_C \sin(\omega t))dt}] \tag{15}$$

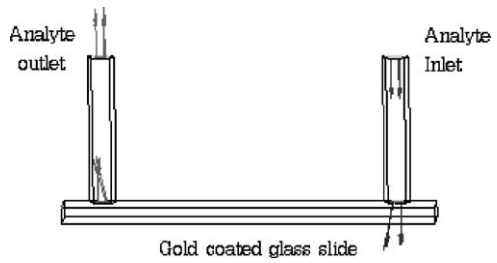

Fig. 2. Schematic illustration of the model system used for the analysis of analyte–receptor binding.

2.1.2. Chemo-mechanical binding analysis

We have developed a finite element computational model for simulating the chemo-mechanical binding of analytes to specific binding molecules on fucntionalized surfaces using CFDRC^{TM} from the CFD Research Corporation. We have conducted simulations using a model where a substrate functionalized with the binding molecules is inserted in a thin plate-shaped flow cell. The simulation system is schematically illustrated in Fig. 2. A liquid solution containing the analyte passes through an orifice with a circular inlet port connecting to the flow cell. A functionalized substrate surface (such as a gold-coated glass-slide) on which the binding molecules are attached is located in the bottom of the flow cell. For the simulations, we have assumed an arbitrary set of analyte and binding moelcues that have a strong binding affinity. The initial analyte concentration in the bulk solution was taken to be 5×10^{-6} M, and the inlet volumetric flow rate was 300 μl/min (Table 1).

Analyte–receptor binding is a very common biological process in nature, which include protein, DNA and protein-DNA interactions. Depending on the chemistry, the binding reaction can be reversible or irreversible. The extent of the binding process depends on the affinity of the analyte to the receptor for chemical reaction, or to the chemical potential of the system. In the presence of multiple analytes and receptors, the binding process can be competitive (different analytes compete for the same receptor) or non-competitive (each analyte binds to a different receptor). The affinity between each individual analyte–receptor complex determines the partitioning of total receptor sites in a competitive binding environment. For the modeling problem considered here, the analyte binds to its receptor forming a reversible analyte–receptor complex indicated with an association rate constant K_a. This complex subsequently dissociates with a rate constant, K_d. This complex again can further form an immobilized complex with a rate constant (K_r)

$$A + B \underset{K_d}{\overset{K_A}{\rightleftarrows}} AB \xrightarrow{K_r} AB^*$$

The distribution of analyte concentration over the reaction surface as a function of time is illustrated in Figs. 3 and 4. After a certain time, when the analyte concentration reaches a saturated level (Fig. 4), the process of binding will reach a state of dynamic equilibrium. The irreversible analyte concentration is uniformly distributed over the reaction surface. This means that the stable chemo-mechanical binding stress gives rise to a uniform distribution for surface stress which can be utilized for bio-sensing using a cantilevered detection system.

Table 1
Various parameters used in the chemo-mechanical binding analysis

Property	Value
Association rate constant, K_a ($M^{-1}\,s^{-1}$)	$1 \times 10^{+9}$
Dissociation rate constant K_d (s^{-1})	0.001
Initial analyte concentration in bulk solution: C_0 (M)	5×10^{-6}
Maximum possible surface analyte concentration P_s ($M\,m^{-2}$)	2×10^{-6}
Density of sample ($kg\,m^{-3}$)	1000
Viscosity of sample ($m^2\,s^{-1}$)	0.86×10^{-6}
Diffusivity of analyte D_e ($cm^2\,s^{-1}$)	4×10^{-7}
Inlet volumetric flow rate Q ($\mu l\,min^{-1}$)	300

2.2. Deflection of the microcantilever due to bimaterial effects

The temperature of the fluid near the microcantilever is expected to vary sinusoidaly with amplitude of ΔT_∞ due

Fig. 3. Distribution of analyte concentration at $t = 5$ s.

Fig. 4. Distribution of analyte concentration at $t = 60$ s.

to oscillations in the flow conditions. Therefore, the thermal lumped analysis predicts the following for the deflection in the microcantilever due to biomaterial effects

$$z_t = \beta_T m\, \Delta T_\infty \frac{m\sin(\omega t) - \omega\cos(\omega t)}{m^2+\omega^2} \tag{16a}$$

where β_T is a constant depending on the thermal expansion coefficient of the two layers of the microcantilever and the relative dimensions of these layers. The parameter m is equal to

$$m = \frac{2h_c \ell w}{c_m m_m} \tag{16b}$$

where h_c, w, c_m and m_m are the convective heat transfer coefficient between the microcantilever and the fluid, width of the microcantilever, specific heat of the microcantilever and the total mass of the microcantilever, respectively. Eq. (16a) suggests that biomaterial effects can be minimized for the conditions where m is very small as for minimum heat transfer convection or for maximum thermal capacitance of the microcantilever.

2.3. Dynamic modeling of the microcantilever

The one degree of freedom model that can best describe the dynamic behavior of the deflection at the tip of the micorcantilever, z_d, due to flow turbulences is shown in the following differential equation:

$$m_e \ddot{z}_d + k_e z_d = \tfrac{1}{2} C_D \rho_l A_e (h_0 \omega F_V)^2 \sin(\omega t) \tag{17}$$

where m_e, k_e, A_e, F_V, h_0 and ρ_l are the effective mass of the cantilever, effective stiffness, effective area of the microcantilever that are subject to flow drag, a velocity correction factor which is the ratio between the magnitude of the velocity at the microcantilever to the velocity magnitude at the source of disturbance which is assumed to be $(h_0\omega)$, characteristic length for the turbulence at its source and the density of the fluid, respectively. The double dot sign represents the second derivative with respect to time. The right side of Eq. (17) represents the drag force excreted by the flow of the fluid on the microcantilever due to oscillating effects. The parameter C_D is the drag coefficient and depends on the geometry of the mirocantlever and the direction of the flow with respect to the microcantlever. The steady periodic solution for Eq. (17) is

$$z_d = \frac{((m_e/k_e)\omega^2)}{1-(m_e/k_e)\omega^2} \frac{0.5\rho_l A_e (h_0 F_V)^2 C_D}{m_e} \sin(\omega t) \tag{18}$$

Eq. (18) suggests that the main parameters that control the dynamical effects are: C_D, F_V, ω/ω_n $(\omega_n = k_e/m_e)$, $\rho_l A_e h_0/m_e$. A decrease in any of these parameters reduces the dynamical effects.

2.4. Effects of turbulence produced by external squeezing

The analysis below is done for flow turbulences that are produced by external noise at the upper plate of the fluidic cell. The studied fluidic cell is considered as a thin film having linearly varying clearance. The lower plate of the fluidic cell is assumed fixed and horizontal while the upper plate is inclined and its vertical motion due to the external noise is assumed to have sinusoidal behavior according to the following relation:

$$h = h_0\left(1 - \delta\cos(\gamma\tau) + \kappa\frac{x}{B}\right) \tag{19}$$

where h_0, κ, δ, τ and B are the reference thickness of the fluidic cell, dimensionless slope of the thin film, upper plate motion amplitude, dimensionless time $(\tau = \omega t)$ and the channel length, respectively. ω, γ and x is a reference vibrational frequency, dimensionless frequency and the horizontal distance starting from the inlet, respectively.

The velocity field, the horizontal dimensionless component U and the vertical dimensionless component V, for the fluid flow inside the fluidic microchannel is shown below which was derived using the reduced continuity equation and Navier Stokes equations for creep flows

$$U(X,Y,\tau) = \frac{u}{(V_0+\omega B)} = \frac{1}{2H}[S\delta\gamma X\sin(\gamma\tau) - (12-S)]\left(\frac{Y}{H}\right)\left(\frac{Y}{H}-1\right) \tag{20}$$

$$V(X,Y,\tau) = \frac{v}{h_0\omega} = \delta\gamma\sin(\gamma\tau)\left[3\left(1-\frac{2\kappa X}{H}\right)\left(\frac{Y}{H}\right)^2 - 2\left(1-\frac{3\kappa X}{H}\right)\left(\frac{Y}{H}\right)^3\right] - 6\left(\frac{12}{S}-1\right)\frac{\kappa}{H}\left[\left(\frac{Y}{H}\right)^3 - \left(\frac{Y}{H}\right)^2\right] \tag{21}$$

where u, v, X, Y and V_0 are dimensional axial velocity, dimensional normal velocity, the dimensional axial distance starting from the inlet normalized by B, the dimensional normal distance starting from the lower plate normalized by h_0 and a reference inlet velocity, respectively. Eqs. (20) and (21) are based on the assumption that the flow rate is constant at the inlet. H is equal to h/h_0 while S is the squeezing number. It is defined as

$$S = \frac{12}{1+V_0/\omega B} \tag{22}$$

where the flow rate at the inlet is equal to $V_0 h_0$. When the microcantilever is placed near the lower plate, $Y/H \approx 0$, then Eqs. (20) and (21) reduces to the following at the exit of the channel

$$U(Y,\tau) = -\frac{1}{2H}[S\delta\gamma\sin(\gamma\tau) - (12-S)]\frac{Y}{H} \tag{23}$$

$$V(Y,\tau) = \left[3\delta\gamma\sin(\gamma\tau)\left(1-2\left(\frac{\kappa}{H}\right)\right) - 6\left(\frac{12}{S}-1\right)\frac{\kappa}{H}\right]\left(\frac{Y}{H}\right)^2 \tag{24}$$

Eq. (24) suggests that F_V can be approximated by the following for fluidic cells having inclined clearances and having the microcantilever set-up placed near the fixed plate

$$F_V \approx 3\left(1-2\left(\frac{\kappa}{H}\right)\right)\left(\frac{Y}{H}\right)^2 \tag{25}$$

Therefore, the ratio of the deflection of the microcantilever due dynamical effects for an inclined channel to that for a flat channel can be approximated by the following for lower amplitudes of the upper plate's vibrations

$$\frac{(z_d)_\kappa}{(z_d)_{\kappa=0}} = \left(\frac{1-\kappa}{1+\kappa}\right)^2 \tag{26}$$

Eq. (26) suggests that dynamical effects on the microcantliever deflection can be reduced for divergent fluidic cells. However, this reduction is prominent near $\kappa = 1$ at relatively low values of δ as shown in Fig. 5. Furthermore, inclined channels create a permanent drag on the microcantlilever because the mean flow will have normal velocity components, the second term in Eq. (24). However, the reduction in the dynamical effects is greater than the deflection due to the induced permanent drag. It is worth noting that the permanent drag can be minimized by aligning the microcantilever along the stream lines.

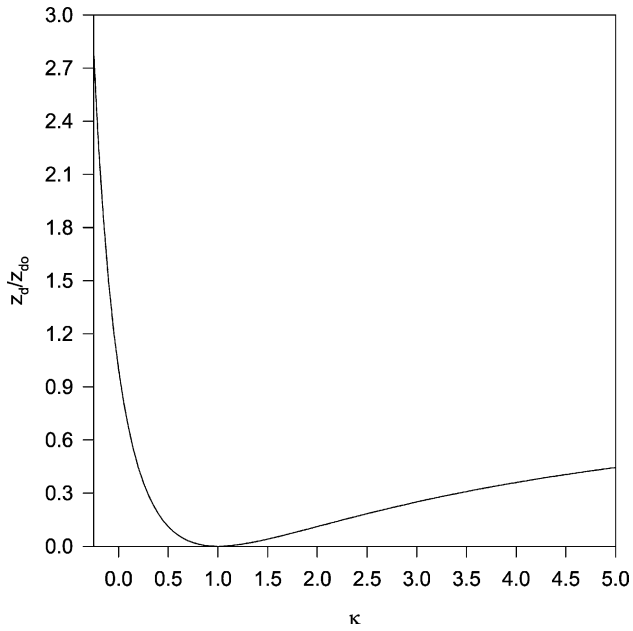

Fig. 5. Effects of κ on $(z_d)_\kappa/(z_d)_{\kappa=0}$.

3. Typical values of cantilevers

The following table lists typical values of the parameters specifying the microcantilever deflection. Note that the data for $(C_\infty)_0 N_r$, $N_r\beta_c$ and $\bar{k}_{fo}$ are extracted from the work of [10] which shows the adhering of lymphoid cells CD8 molecules into anti-CD8-coated surface by a shear flow.

The parameters a and b are assumed due to lack of experimental values (Table 2).

Figs. 6 and 7 describe the effects of the dimensionless slope κ on translational and normal velocities, normalized with respect to V_0, at the exit for two different times, respectively. They are based on the fact that the microcantilever is placed near the lower plate in the presence of an

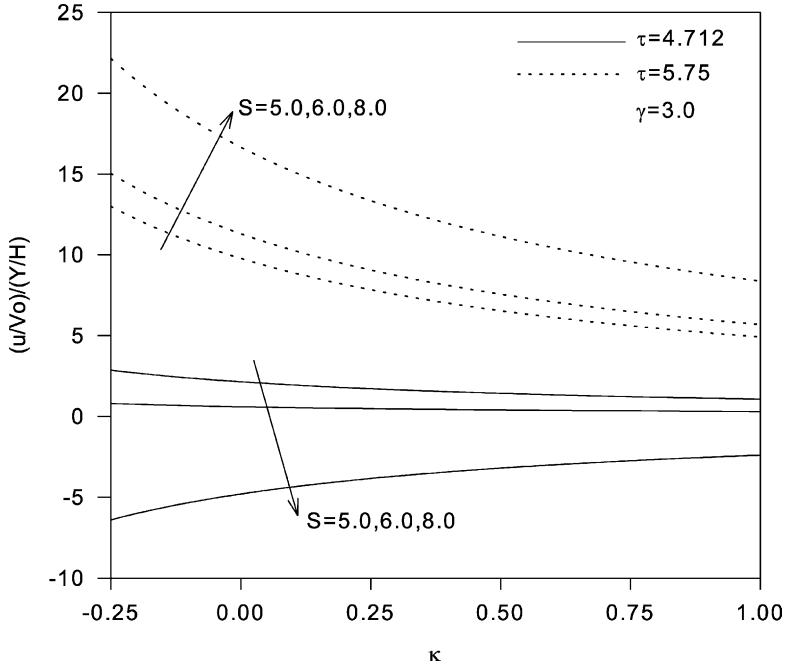

Fig. 6. Effects of κ on $(u/V_0)1/(Y/H)$.

Table 2
Typical values of the parameters specifying the microcantilever deflection

Material	Properties (Si_3N_4 coated with thin layer of gold)
ℓ (μm), w (μm), t_m (nm)	120, 40, 50
m_m (kg), m_e (kg)	5.59 (10^{-13}), 1.34 (10^{-13})
k_e (N/m), ρ (kg m^{-3}), $(C_\infty)_0 N_r$ (μm^{-2})	0.06, 2330, 410 1
z_0 (nm), h_0 (mm), B (mm)	50, 0.4, 70
δ, $N_r\beta_c$ (μm^{-2})	0.3, 82
h_0 (mm), F_V, Y/H, V_0 (m/s)	0.2, 0.2, 0.1, 0.05
$\bar{k}_{fo}$ (μm^2/s), a (s)	17.1(10^{-5}), 0.1
m (s^{-1}), κ	100, 0.0 (unless stated)
C_D, ρ_l (kg/m^3), A_e (ℓw)	1.0, 800, 0.5

external sinusoidal noise at the upper plate. The values of $\tau = 4.712$ and $\tau = 5.75$ represent the cases when the upper plate reaches its maximum relief and squeezing speeds, respectively. It is noticed that the absolute value of the translational velocity decrease with increases in κ. This will result in increasing the adhesion rate. Increases in the squeezing number S can cause reductions and enhancements in rolling velocities during relief (as long as the flow is not reversed) and squeezing stages, respectively. S increases by increases in the turbulence frequency. Variations in normal velocities are noticed to decrease as κ increases (Fig. 7).

Fig. 8 shows the deflection spectrum of the microcantilever due to surface stress at $t = 5$ s. The deflection at relatively small values of ω is mainly influenced by the noise in the analyte concentration near the microcantilever. In this region, the noise in the deflection spectrum is clearly recognized as shown in Fig. 8. At large values of ω, the deflection is found to increase smoothly until reaching an asymptotical value for the selected parameters. This behavior is mainly due to increases in the vibrational frequency of the analyte molecules as ω increases when the effects of the rolling velocities on the binding are small, otherwise the deflection will decrease. The spectrum for the intermediate region of ω contains small noise levels due to the interference between the effect of the noise in the concentration and vibrational/rolling effects of the analyte molecules. Decreases in the deflection are noticed as b increases due to increases in the rolling velocity effects. At relatively large frequencies, bimaterial effects on the deflection decreases as shown in Fig. 9.

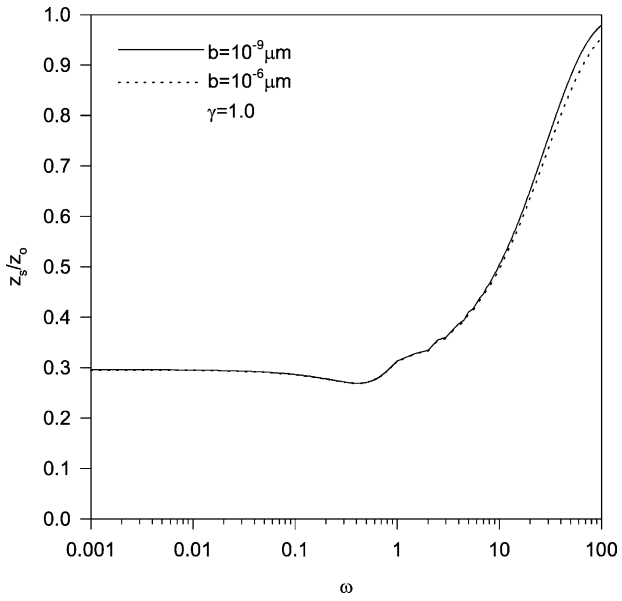

Fig. 8. Effects of ω on z_s/z_0 at $t = 5$ s.

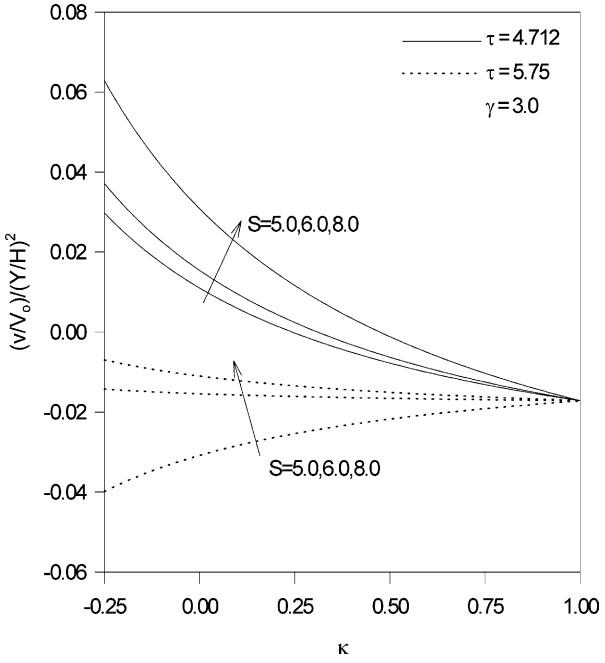

Fig. 7. Effects of κ on $(v/V_0)(1/(Y/H)^2)$.

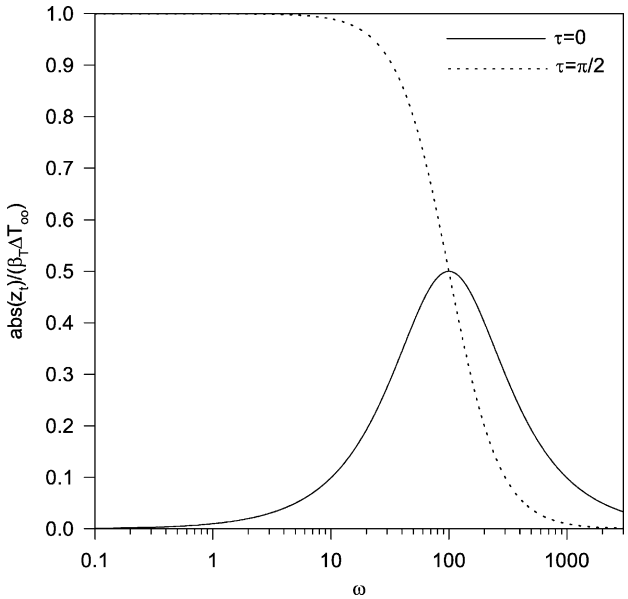

Fig. 9. Effects of ω on $|z_t|/\beta_T \Delta T_\infty$.

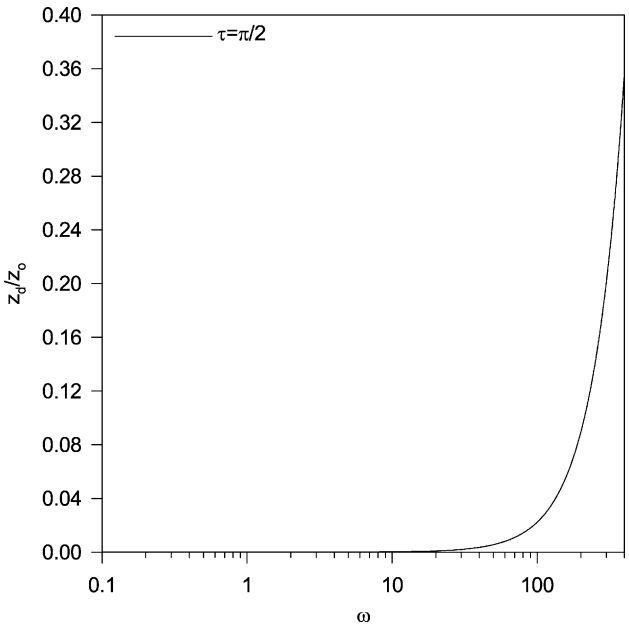

Fig. 10. Effects of ω on z_d/z_0.

Although, the deflection of the microcantilever is enhanced at large frequencies, the noise due to dynamical disturbances on the microcantliever increases drastically as shown in Fig. 10. With regards to bimaterial effects, they can be reduced by geometrical considerations for the chamber such as using convergent chambers or using special coolers as in the works of [14]. This reduction can also be accomplished by comparing the deflection of the microcantilever with an idle one to eliminate these effects as illustrated in the work of [3].

4. Different cantilever assemblies

It was found that oscillations in flow conditions can enhance the detection of the microcantilever in the absence of the dynamic effects of the flow. Therefore, it is suggested to have new generations of microcantilevers that are less sensitive to turbulence and have enhanced deflections. Below are few designs for the microcantilever assembly. Assembly (a) and (b) of Fig. 11 have a large effective stiffness hence lower turbulence effects. Also, they have larger deflection as compared to an ordinary microcantilever. Specifically, there is a substantial enhancement in deflection at the mid point of the connecting beam for assembly (a) and at the free end of the intermediate beam and for assembly (b). The receptor coatings on the connecting and intermediate beams for assemblies (a) and (b), respectively, are on the opposite surface to those for the other beams where their receptor coatings are on one side as shown in Fig. 11. Assembly (c) will be subjected to lower drag amplitude than the ordinary microcantilever because it is close to the wall (has lower F_V values).

Assembly (d) is an ordinary microcantilever with the receptor coating being placed on one half of the upper surface of the microcantilever and along the opposite half of the lower surface of the microcantilever as shown in Fig. 11. Further, this microcantilever has a long slit along the interface between the receptor coating and the surface that is free from receptor as shown in Fig. 11. This slit allows the separated sides of the microcantilever to have deflections in opposite directions upon analyte bindings with the receptors on the shown alternating surfaces. The analyte concentration can then be related to the opening of the slit Δz_s. The opening is almost unaffected by dynamical effects because both surfaces are subjected to almost similar flow drags.

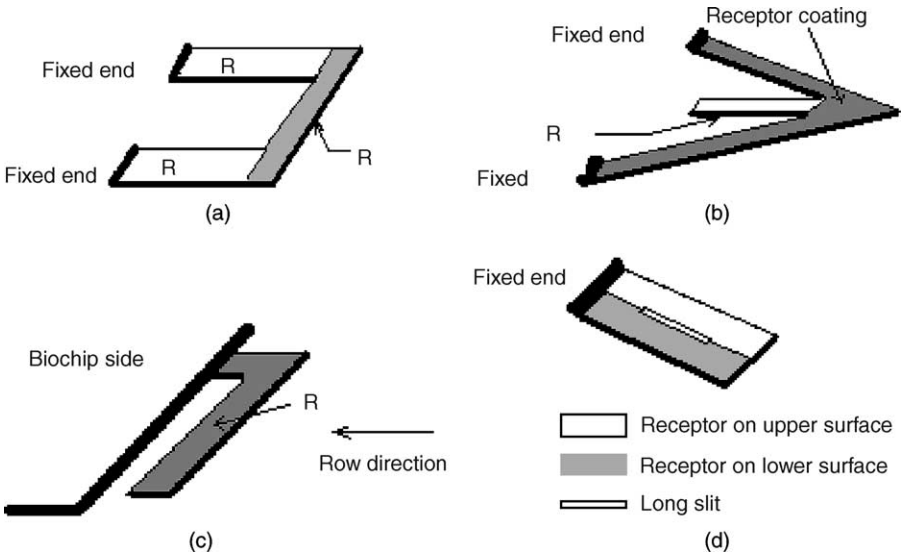

Fig. 11. Suggested different designs of the microcantilever assembly.

Table 3
Summary of the performance of the different microcantilever assemblies

z	Ordinary M/C	Assembly (a)	Assembly (b)	Assembly (c)	Assembly (d)
Maximum z_s	z_0 M/C length $= L$	1.25 z_0 beam length $= L$	$\approx$2.0 z_0 intermediate beam length $= L$	z_0 total length $= L$	$\Delta z_s < z_0$ slit length $= L$
z_t	z_{to}	1.25 z_{to}	$\approx$2.0 z_{to}	1.0 z_{to}	$\Delta z_t < z_{to}$
z_d	z_{do}	$<z_{do}$ at low ω	$<z_{do}$ at low ω	$<z_{do}$	$\approx$0

Table 3 shows a comparison between the suggested microcantilever assemblies and the ordinary microcantilever, M/C, according to their corresponding values of z_s, z_t and z_d. Note that the length of the intermediate beam for assembly b is assumed to extend to the fixed end.

5. Design and optimization of piezoresistive cantilevers

In this section, we discuss the mechanical design and optimization of piezoresistive cantilevers for use in detecting changes in surface stress upon analyte-receptor binding. The fractional change in resistance ($\Delta R/R$) of a piezoresistive cantilever is described by the following expression,

$$\frac{\Delta R}{R} = \beta \frac{3\pi_L(1-\upsilon)}{t_m}(\sigma_1 - \sigma_2)$$

where π_L is the piezoresistive coefficient of Silicon along the $\langle 1\,1\,0\rangle$ axis, σ_1 is the longitudinal stress, σ_2 the transverse stress, t_m the thickness of the cantilever, and β a factor that adjusts for the thickness of the piezoresistor [15]. From the above expression, the ($\Delta R/R$) ratio is proportional to the stress difference ($\sigma_1 - \sigma_2$). The stress difference distribution depends on the geometric factors of the layers and the chemo-mechanical forces between the biomolecules and the capture or hybridization layers. Therefore, the deflection signal can be increased by maximizing the stress difference ($\sigma_1 - \sigma_2$) in the way of changing the geometric factors. In addition, the method of stress concentration regions (SCR) can be employed (as discontinuity holes) to further increase this stress difference, giving rise to an increased sensitivity in biodetection. Furthermore, the use of a double cantilever arrangement can increase the amount of "large stress difference area".

Modeling and simulations for piezoresistive cantilevers were conducted using the CFDRC^{TM}. The cantilever beam was assumed to be 40 μm in width and 150 μm in length. In addition, the length of the piezoresistive layer was taken to be 100 μm. For the properties of the piezoresistive layer, we have utilized the parameters of the PZT-8 system from Morgan Matroc, Inc. [17] The following matrices represent the piezoressitivity parameters of the PZT-8 system.

The 3D dielectric matrix (F/m)

$$[\varepsilon] = \begin{bmatrix} 8003 & 0 & 0 \\ 0 & 8003 & 0 \\ 0 & 0 & 2252 \end{bmatrix} \times 10^{-9}$$

The 3D piezoelectric matrix (C/m^2)

$$[D] = \begin{bmatrix} 0 & 0 & -388 \\ 0 & 0 & -388 \\ 0 & 0 & 1391 \\ 0 & 0 & 0 \\ 0 & 1034 & 0 \\ 1034 & 0 & 0 \end{bmatrix}$$

All three simulations were conducted with the same conditions of analyte concentration and the same analyte capturing area. For the double cantilever beam arrangement, the capture area was designed to be the whole area of the connection beam. For the regular piezoresistive cantilever as shown in Fig. 12, the quantity of stress difference ($\sigma_1 - \sigma_2$) is maximized near the cantilever beam support area as expected. Fig. 13 shows the integrated value of ($\sigma_1 - \sigma_2$) over the length of the cantilever where over the capture area, the value of ($\sigma_1 - \sigma_2$) is constant around 0.06 MPa. Towards the beam support area, the value of ($\sigma_1 - \sigma_2$) increases to around 0.1 MPa. For the case of a single piezoresistive cantilever with SCR as shown in Fig. 14, The value of ($\sigma_1 - \sigma_2$) further increases near the support area reaching a maximum value of 0.6 MPa over a plateau, that is, 30 μm in length (Fig. 15). This would be the optimum region for placing the piezoelectric layer to collect sufficiently large displacement signals. For the double piezocantilever arrangement with SCRs in Fig. 16, the maximum value of the stress difference increases to nearly 1 MPa, and the length of the "flat roof" area increases to 60 μm, which means that the effective signal collecting area is further increased (Fig. 17).

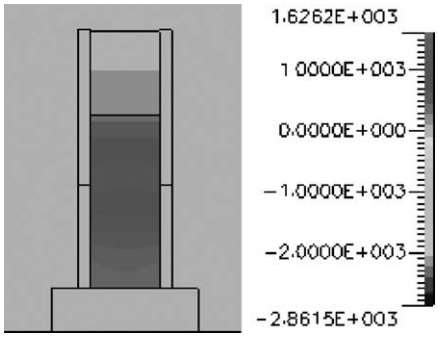

Fig. 12. Distribution of stress difference ($\sigma_1 - \sigma_2$) in a piezoresistive cantilever beam.

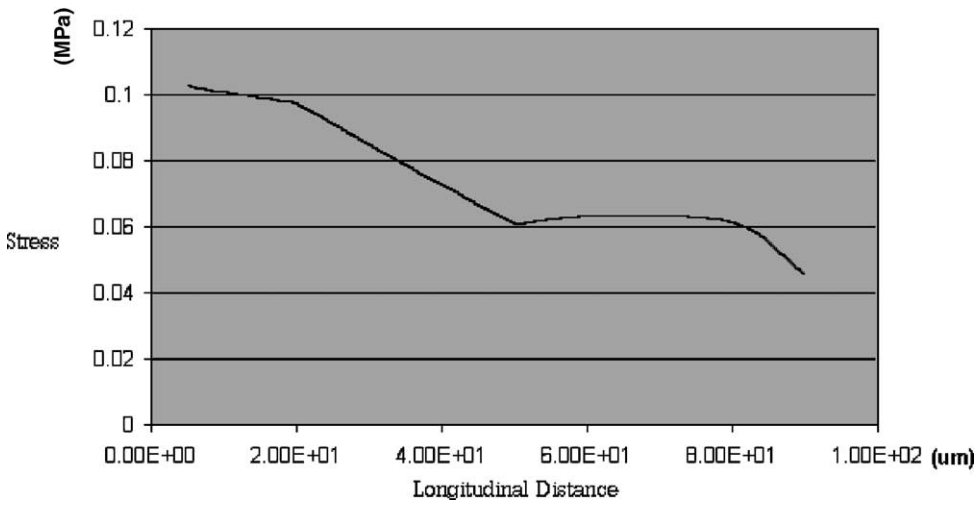

Fig. 13. Integrated stress difference along the longitudinal axis of the cantilever beam.

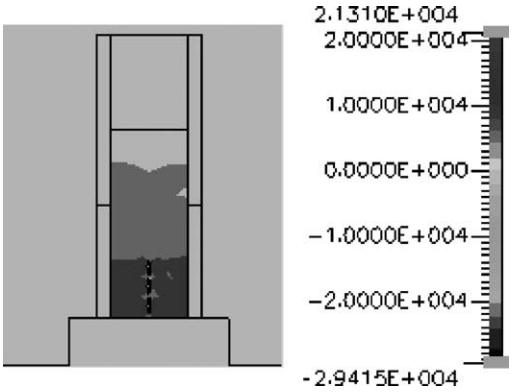

Fig. 14. Distribution of stress difference in a piezoresistive cantilever with SCR's.

6. Biodetection based on resonance frequency shift

In this section, we present results from experiments where we utilized the resonance frequency shift of micro-cantilever beams for biosensing. For our experiments, we have used commercially available silicon microcantilevers for biosensing from Thermomicroscopes, Inc., Sunnyvale, CA (ultralevers, types A, B, C and D) whose properties are provided in Table 4. The changes in the resonance frequency of the cantilevers were detected optically using an atomic force microsopy system (CP-Research, Thermomicroscopes Inc.).

Microcantilevers are mounted to a cartridge with a piezoresistive film stack for operation in the non-contact or tapping mode. An optical detection system with a four-quadrant photodetector is used to detect the cantilever detection and the resoance frequency. The ultralevers have a

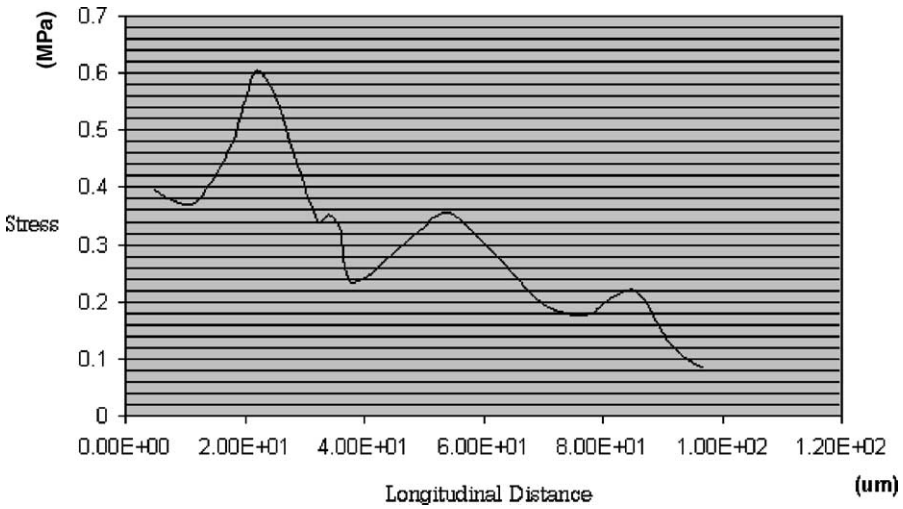

Fig. 15. Integrated stress difference along the longitudinal axis of the cantilevers with SCR's.

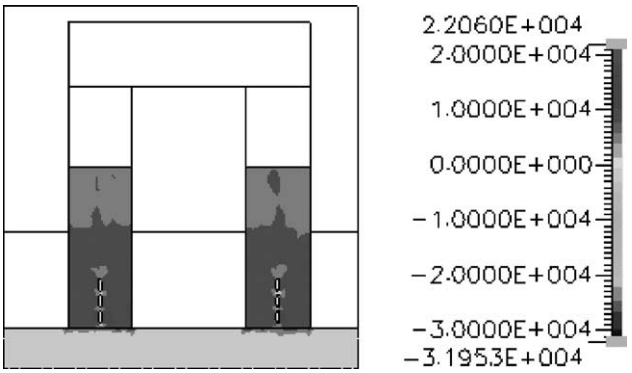

Fig. 16. Distribution of stress difference for the double piezocantilever arrangement.

gold coating on the backside for enhanced surface reflectivity, which is also useful for chemical modification to obtain selective binding of specific analytes. For our experiments, self assembled monolayers (SAM) of aminoethanethiol and dodecanethiol were utilized as receptor molecules to modify the cantilever surface. The sulfur group in the thiol chain has high affinity for binding to gold surfaces and hence well defined monolayers are generated, which are dense and stable [3,16]. Before doing the chemical modification, we have measured the blank cantilever's frequency response (first-order resonance) using our AFM in the non-contact mode. Chemical modification was achieved by dipping the cantilevers into saturated solutions of aminoethanethiol and dodecanethiol for a duration of 12 h, followed by a 24 h drying process. After that, the modified cantilever's frequency response was recorded.

The height of the aminoethanethiol and dodecanethiol self assembled monolayers were taken to be 8 and 20 Å, respectively. Compared to the thickness of the cantilever beam (1.8 μm), these SAMs are considered to be ultra thin films [8]. When a cantilever beam is coated with a thin film, the flexural rigidity will change, and the change in stiffness as well as the mass will directly affect the resonance frequency of the beam's vibration. The stiffness change will be reflected as a change in the force (cantilever bending) versus distance (scanner extension) curve of the cantilever, which is directly obtained from AFM, and the slope of the linear portion of the curve is inversely proportional to the stiffness of the cantilever.

A cantilever beam is considered to be a long, thin beam with one end fixed and the other end being free. Assuming the cantilever behaves linearly elastic and uniform in dimension, and only a small deflection is issued, the resonance frequency of the beam ω_n can be determined by

$$\omega_n = {k_n}^2 \sqrt{\frac{EI}{\lambda}}$$

where k_n is constant, EI the flexural rigidity, E the elastic modulus, I the moment of inertia, and λ the linear density of

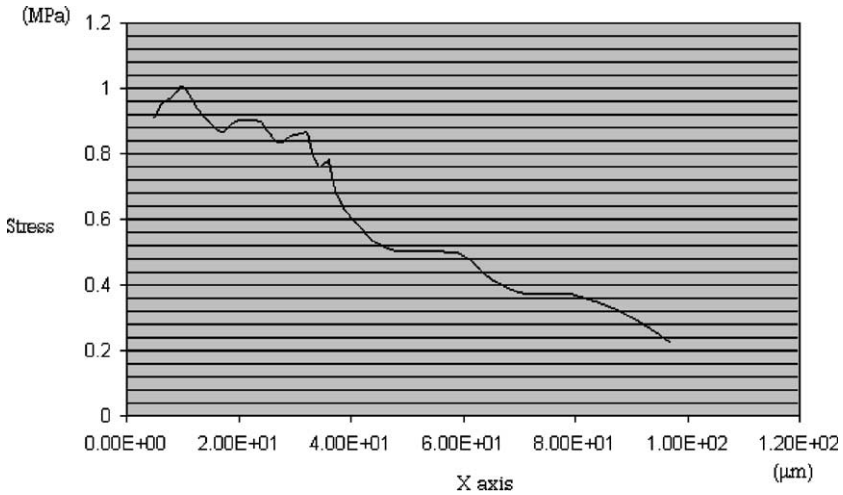

Fig. 17. Integrated stress difference along the longitudinal axis for the double piezocantilever arrangement.

Table 4
Geometrical and physical parameters of the cantilevers used in the experiments

Type	L (μm)	W (μm)	Typical thickness (μm)	Typical force constant (N/m)	Typical resonance frequency (kHz)
UL20A	180	25	1.8	1.9	53
UL20B	180	38	1.8	2.8	64
UL20C	85	18	1.8	13	300
UL20D	85	28	1.8	18	360

the beam. After the surface modifications, the characteristics of the cantilever beam change due to the formation of the self assembled monolayer. The linear mass density of the modified cantilever will become,

$$\lambda_c = \rho_s A_s + \rho_f A_f$$

and its flexural rigidity will be redefined as,

$$EI = E_s I_s + E_f I_f$$

where 's' represents the substrate that the beam is fabricated from and 'f' represents the self assembled monolayer. In addition, the modified center of mass of the cantilever is given by,

$$y_{cm} = \frac{E_s h_s^2 + E_f(2h_s h_f + h_f^2)}{2E_s h_s + 2E_s h_f}$$

The moment of inertia of the modified beam will also change to

$$I_s = \frac{w h_s^3}{12} + w h_s \left(y_{cm} - \frac{h_s}{2} \right)^2$$

$$I_f = \frac{w h_f^3}{12} + w h_f \left(\frac{h_f}{2} + h_s - y_{cm} \right)^2$$

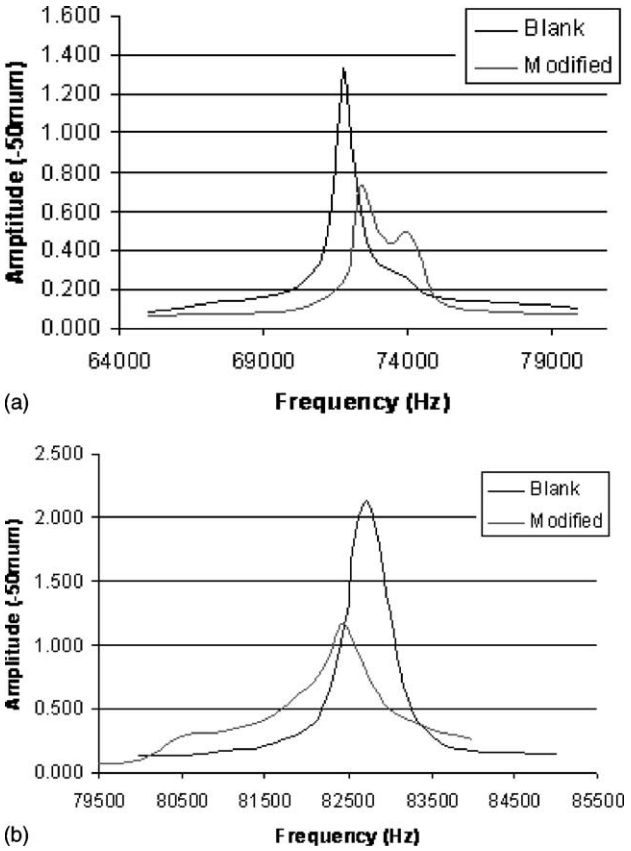

Fig. 18. Frequency response before and after modification, for (a) aminoethanethiol SAM, (b) dodecanethiol SAM.

Consequently, the new resonance frequency and the frequency shift are given by the following expressions:

$$\omega_c = k_n^2 \sqrt{\frac{E_s I_s + E_f I_f}{\lambda_c}}$$

$$\Delta\omega_c = k_n{}^2 \left[\sqrt{\frac{E_s I_s + E_f I_f}{\lambda_c}} - \sqrt{\frac{EI}{\lambda}} \right]$$

These equations show that both the stiffness and the mass loading affect the resonance frequency of the cantilever [7]. Figs. 18(a and b) show the results of resonance frequency change measured using ultralevers of type B (Table 4) for aminoethanethiol and dodecanethiol coatings respectively. For the case of aminoethanethiol coating in Fig. 18(a), we have observed an increase in the resonance frequency while the resonance frequency dropped for the case of dodecanethiol coating in Fig. 18(b). Fig. 19 shows the force vs. deflection curves for both SAMs. We see that while for the case of aminoethanethiol coating the stiffness of the cantilever has increased, a little change was observed in the case of dodecanethiol coating. An aminoethanethiol has a hydrochloride group at the end which leaves a proton upon salvation. The charged end of aminoethanethiol molecules can interact via van der Waals forces to form highly rigid three dimensional networks. In addition, the amino group of the molecule is oriented at a non-coplanar angle to the

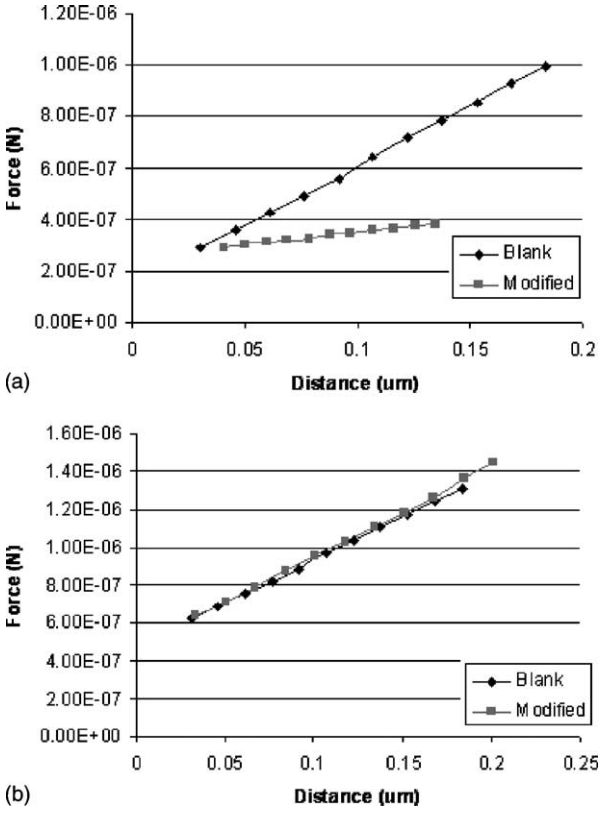

Fig. 19. Force vs. distance curves for the case of (a) aminoethanethiol and (b) dodecanethiol coatings.

carbon backbone. Furthermore, dodecanethiol is a highly linear molecule and can form dense and pitless monolayers. Therefore, a self assembled monolayer of aminoethanethiol has a lower density compared to that of a dodecanethiol layer. Hence, the mass of the dense monolayer of dodecanethiol has a more dominant effect on the frequency shift: when the stiffness change for the cantilever is neglicible, mass loading dominates the shift in the resonance frequency of the cantilever.

7. Summary and conclusions

The deflection of the microcantilevers due to chemical reactions and biomaterial and turbulence effects were analyzed. Analysis of the bimaterial effects on the microcantilever revealed its influence on the deflection especially at low turbulence frequency. In the absence of bimaterial effects, turbulence was found to increase the deflection due to chemical reactions only at large frequencies yet it increases the noise due to the increased dynamical effects of the flow on the microcantilever. Deflections of microcantilevers are found analytically to be enhanced while turbulence effects are found to be minimized for certain configurations of the microcantilever assemblies. Finite element modeling for piezoresistive cantilevers has shown that detection sensitivity can be increased by tailoring the properties of the piezoresistive layer and by introducing stress concentration regions to enhance the surface stresses. Reductions in dynamical effects on the microcantilever were found to be possible for divergent fluidic cells. Experiments based on resonance frequency shifts show that the biodetection process is strongly influenced by the interaction of analytes with the receptor substrate. Current efforts are underway for fabricating functionalized monolayers that will act as platforms for specific attachment of receptors or pathogens for selective bio-sensing applications.

Acknowledgements

We acknowledge support of this work by DOD/DARPA/DMEA under grant number DMEA 90-02-2-0216.

References

[1] T. Vo-Dinh, B.M. Cullum, D.L. Stokes, Nanosensors and Biochips: Frontiers in Biomolecular Diagnostics, Sens. Actuators B 74 (2001) 2–11.
[2] R. Raiteri, G. Nelles, H.-J. Butt, W. Knoll, P. Skladal, Sensing of Biological Substances Based on the Bending of the Microfabricated Cantilevers, Sens. Actuators B 61 (1999) 213–217.
[3] J. Fritz, M.K. Baller, H.P. Lang, H. Rothuizen, P. Vettiger, E. Meyer, H.-J. Güntherodt, Ch. Gerber, J.K. Gimzewski, Translating Biomolecular Recognition into Nanomechanics, Science 288 (2000) 316–318.
[4] H. Jensenius, J. Thaysen, A.A. Rasmussen, L.H. Veje, O. Hansen, A. Boisen, A mircrocantilever-based alcohol vapor seonsor-application and response model, Appl. Phys. Lett. 76 (18) (2000) 2615–2617.
[5] A. Boisen, A.G. Hansen, J. Thaysen, H. Jensenius, O. Hansen, Environmental sensors based on micromachined cantilevers with integrated read-out, Ultramicroscopy 82 (1-4) (2000) 11–16.
[6] A.G. Hansen, M.W. Mortensen, J.E.T. Anderson, J. Ulstrop, A. Kuhle, J. Garnaes, A. Boisen, Stress formation during self-assembly of alkanethiols on differently pre-treated gold surfaces, Probe microscope 2 (2001) 139–149.
[7] P. Lu, F. Shen, S.J. O'shea, K.H. Lee, T.Y. Ng, Analysis of surface effects on mechanical properties of microcantilevers, Mater. Phys. Mench. 4 (2001) 51–55.
[8] A.M. Moulin, S.J. O'Shea, M.E. Welland, Microcantilever-based biosensors, Ultramicroscopy 82 (2000) 23–31.
[9] N.V. Lavrik, C.A. Tipple, M.J. Sepaniak, D. Datskos, Gold nanostructure for transduction of biomolecular interactions into micrometer scale movements, Biomed. Microdevices 3 (1) (2001) 35–44.
[10] K.-C. Chang, D.A. Hammer, The forward rate of binding of surface-tethered reactants: effect of relative motion between two surfaces, Biophys. J. 76 (1999) 1280–1292.
[11] D.G. Swift, R.G. Posner, D.A. Hammer, Kinetics of adhesion of IgE-sensitized rat basophilic leukemia cells to surface-immobilized antigen in Couette flow, Biophys. J. 75 (1998) 2597–2611.
[12] A. Ramakrishnan, A. Sadana, A predictive approach using fractal analysis for analyte-receptor binding and dissociation kinetics for surface plasmon resonance biosensor applications, J. Interf. Colloid Sci. 229 (2000) 628–640.
[13] W.F. Pritchard, P.F. Davis, Z. Derafshi, D.C. Polacek, R. Tsoa, R.O. Dull, S.A. Jones, D.P. Giddens, Effects of wall shear stress and fluid recirculation on the localization of circulating monocytes in a three dimensional flow model, J. Biomech. 28 (1995) 1459–1469.
[14] G. Wu, H. Ji, K. Hansen, T. Thundat, R. Datar, R. Cote, M.F. Hagan, A.K. Chakraborty, A. Majumdar, Origin of nanomechanical cantilever motion generated from biomolecular interactions, PNAS 98 (2001) 1560–1566.
[15] J.A. Harley, T.W. Kenny, High-sensitivity cantilevers under 1000A thick, Appl. Phys. Lett. 75 (2) (1999) 89–291.
[16] A. Ulman, Formation and structure of self assembled monolayers, Chem. Rev. 96 (1996) 1533–1554.
[17] Piezoelectric Technology Data for Designers, Morgan Matroc Inc., Electro Ceramics Division, 2000, p.14.